Chemical Science

ROYAL SOCIETY OF CHEMISTRY

EDGE ARTICLE

View Article Online
View Journal | View Issue

Cite this: *Chem. Sci.*, 2024, **15**, 10529

All publication charges for this article have been paid for by the Royal Society of Chemistry

The interplay of covalency, cooperativity, and coupling strength in governing C–H bond activation in Ni_2E_2 (E = O, S, Se, Te) complexes†‡

Sunita Sharma, Bhawana Pandey and Gopalan Rajaraman *

Dinickel dichalcogenide complexes hold vital multifaceted significance across catalysis, electron transfer, magnetism, materials science, and energy conversion. Understanding their structure, bonding, and reactivity is crucial for all aforementioned applications. These complexes are classified as dichalcogenide, subchalcogenide, or chalcogenide based on metal oxidation and coordinated chalcogen, and due to the associated complex electronic structure, ambiguity often lingers about their classification. In this work, using DFT, CASSCF/NEVPT2, and DLPNO-CCSD(T) methods, we have studied in detail $[(NiL)_2(E_2)]$ (*L* = 1,4,7,10-tetramethyl-1,4,7,10-tetraazacyclododecane; E = O, S, Se and Te) complexes and explored their reactivity towards C–H bond activation for the first time. Through a comprehensive analysis of the structure, bonding, and reactivity of a series of $[(NiL)_2(E_2)]$ complexes with E = O, S, Se, and Te, our computational findings suggest that $\{Ni_2O_2\}$ and $\{Ni_2S_2\}$ are best categorised as dichalcogenide-type complexes. In contrast, $\{Ni_2Se_2\}$ and $\{Ni_2Te_2\}$ display tendencies consistent with the subchalcogenide classification, and this aligns with the earlier structural correlation proposed (Berry and co-workers, *J. Am. Chem. Soc.* 2015, 137, 4993) reports on the importance of the E–E bond strength. Our study suggests the reactivity order of $\{Ni_2O_2\}$ > $\{Ni_2S_2\}$ > $\{Ni_2Se_2\}$ > $\{Ni_2Te_2\}$ for C–H bond activation, and the origin of the difference in reactivity was attributed to the difference in the Ni–E bond covalency, and electronic cooperativity between two Ni centres that switch among the classification during the reaction. Further non-adiabatic analysis at the C–H bond activation step demonstrates a decrease in coupling strength as we progress down the group, indicating a correlation with metal–ligand covalency. Notably, the reactivity trend is found to be correlated to the strength of the antiferromagnetic exchange coupling constant *J via* developing a magneto-structural-barrier map – offering a hitherto unknown route to fine-tune the reactivity of this important class of compound.

Received 30th April 2024
Accepted 31st May 2024

DOI: 10.1039/d4sc02882a

rsc.li/chemical-science

Introduction

Transition metal ions are integral to oxidation and electron transfer processes in nature, as well as in the realms of industrial and academic chemistry.[1–4] The high valent metal-oxo or hydroxo functional groups participate in a series of electron transfer processes in biological and chemical events. Because of their wide significance in biological and chemical sciences, an immediate issue is determining the reactivity differences among these related active transition metal ion species and understanding their roles in various oxidation processes. Iron,[5–7] manganese,[8,9] and copper[10,11] ion-containing metalloenzymes are very popular, but other metal ions also play an important role in biological chemistry. The study of these complexes helps us better understand the detailed mechanism of the reaction catalysed by metalloenzymes and gives an idea for developing a biomimetic catalyst.[12]

Apart from the aforementioned metal ions, the studies on nickel complexes are also essential in metalloenzyme chemistry[13] due to their involvement in various biological reactions and homogenous catalysis.[14,15] Nickel enzymes play important roles in the global biological carbon, nitrogen, and oxygen cycle. Some examples, including hydrogenases,[16,17] Ni-SOD,[18–20] urease,[21,22] glyoxalase,[23] CO dehydrogenase,[24] *etc.*, are a few examples of metalloenzymes containing nickel ions in the active sites. In comparison to Ni^{II} chemistry, dealing with the Ni^{III} oxidation state poses a greater challenge in nickel chemistry, primarily due to the complexity involved in synthesizing and characterizing Ni^{III} complexes.[24,25] Many homo- and hetero-metallic oxo-bridged Ni complexes have been reported, but only a few high-valent metal oxo species have been characterised well so far.[26] Moro-oka and co-workers have studied the synthesis and characterisation of the thermally unstable dinuclear bis(μ-oxo)Ni^{III}-complex $[Tp^{Me_3}Ni(\mu\text{-}O)_2NiTp^{Me_3}]$.[27] Although five coordinated Ni^{III} complexes were reported, later they synthesised a new doubly oxo bridged six coordinated bis(μ-oxo)nickel(III)

Department of Chemistry, Indian Institute of Technology Bombay, Mumbai, 400076, India. E-mail: rajaraman@chem.iitb.ac.in

† Dedicated to the 65th birthday of Prof. M. S. Balakrishna, IIT Bombay, India.

‡ Electronic supplementary information (ESI) available. See DOI: https://doi.org/10.1039/d4sc02882a

complex, $[Ni_2(\mu\text{-}O)_2(Me_3\text{-}tpa)_2]^{2+}$.[28] Mitra and co-workers[29] have reported a thermally stable mono-oxo bridged dinuclear Ni^{III} complex, $[Ni(salen)_2O]$, and crystallographic studies on that complex show distorted square pyramidal geometry around the metal ion. These high-valent bis-μ-oxo dimers having an $\{M_2(\mu\text{-}O)_2\}$ core, *i.e.*, a diamond core structure, have tremendous applications in oxidation catalysts.[28,30,31] Monomeric nickel-oxo is very rare because of the tendency of the oxo and hydroxo ligands to form a bridge.[32] Metal complexes with terminal oxo[7,33] or hydroxo ligands have been implicated in various oxidative transformations, such as C–H bond functionalisation and oxo–transfer reactions.[34–36] Several bio-inspired catalysts have been probed as a catalyst for hydroxylation, sulfoxidation, and epoxidation.[37–40] It is assumed that this species has high relevance to the $(\mu\text{-}\eta^2\text{:-}\eta^2\text{peroxo})Cu_2$ complex.[30]

Metals containing not only oxygen but other chalcogen ligands, such as S, Se, and Te have fascinated researchers because of their unique structural properties, bonding, catalytic reactivity, and synthetic applications.[41,42] These complexes have biological significance as well.[43,44] In the case of sulfur-containing complexes, metalloproteins usually consist of metal sulfur bonds. Several metalloproteins contain nickel in the active site, ligated with sulfur such as acetyl-CoA synthase/carbon monoxide dehydrogenase (ACS/CODH),[45,46] [NiFe] hydrogenase,[47] nickel superoxide dismutase,[48] and methyl-CoM reductase.[49] In 2010, Brunold and co-workers studied $[\{(PhTt^{tBu})Ni^{II}\}_2(\mu\text{-}\eta^2\text{:}\eta^2\text{-}S_2)]$ ($PhTt^{tBu}$ = phenyltris[(*tert*-butylthio)methyl] borate) complex of nickel-containing thioether chelating ligand with a tridentate monoanionic $PhTt^{tBu}$ ligand.[50,51]

Notably, nickel oxygen and nickel sulfur complexes have been synthesised and structurally characterised. But corresponding chemistry of the heavier dichalcogenides *viz.* Se_2, Te_2 is substantially unexplored. In 2001, Sitzmann and co-workers, reported the formation of the dimers $[\{(C_5HR_4)NiE\}_2]$ (E = S, Se, Te) by the reaction of dimeric cyclopentadienylnickel bromide derivative $[\{(C_5HR_4)Ni(i\text{-}Br)\}_2]$ with sodium dichalcogenides Na_2E_2.[52] The structure predicts unusual E···E distance giving rise to ambiguities in the description of their electronic structure and chemical reactivity. Three bonding modes are proposed for the Ni_2E_2 core (E = O, S, Se, and Te; see Fig. 1), and the bonding modes are directly correlated to their oxidation states and hence their reactivity.[53–56] In 2012, Berry and co-workers studied a $[(Cp'Ni)_2(\mu_2\text{-}Se_2)]$ (Cp' = 1,2,3,4 tetraisopropylcyclopentadiene) complex by means of X-ray absorption spectroscopy, X-ray, and theoretical methods and predicted bonding mode in Ni_2E_2 as "subselenide" Se_2^{3-} ligand.[54] Although rare, Ni–Se bonding also has biological implications wherein [NiFeSe] hydrogenases were found to be more reactive compared to [NiFe] hydrogenases containing cysteine sulphur group and terminal side-on {Se–S} bonding with Ni atom likely to cause greater reactivity.[57] The reactivity of NiSe dichalcogenide complexes has been of interest since then, and in this regard, a report by Riordan and co-workers on a rare C–H bond activation by a dinickel dichalcogenide complex $[(NiL)_2(Se_2)](PF_6)_2$ (here, L = 1,4,7,10-tetramethyl-1,4,7,10-tetraazacyclododecane) having planar $Ni_2(\mu\text{-}\eta2\text{:-}\eta^2Se_2)$ core structure gains attention. Particularly, this compound was found to oxidise the C–H bonds of DHA and CHD, yielding aromatic product and hydroselenide, demonstrating a scarce C–H bond activation by $\{Ni_2Se_2\}$ compound.[58]

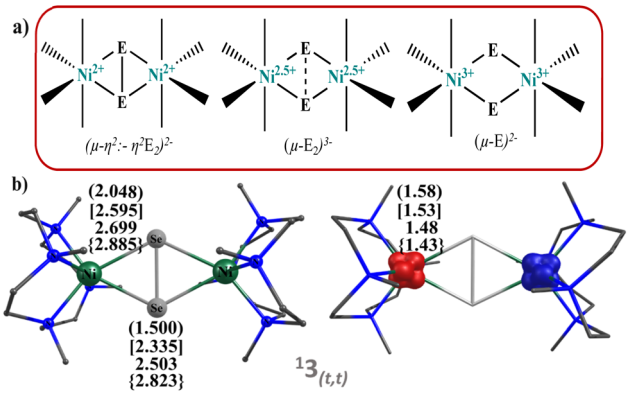

Fig. 1 (a) Schematic representation of all the three possible bonding modes preferred by dichalcogenides (E_2) to the dinuclear metal complexes (b) DFT optimised geometries and spin density plots of complexes $^1\mathbf{3}_{(t,t)}$. The curve, square and curly brackets are for **1**, **2** and **4**, respectively.

Although there are several reports on the structure and bonding of Ni_2E_2 species, comparative analysis across the periodic table from O, S, Se, to Te is lacking and is important given the recent trend of greater reactivity shown by the later dichalcogenide complexes. Further, the reactivity of these species with respect to their bonding has not been studied as all the reports were restricted to the ground state energy of the structure where the E···E distances are constant. If we consider the C–H bond activation of these species, the E···E distance is expected to vary. Hence, various forms of the structure described in Fig. 1 are expected to play a role in enhancing/diminishing the reactivity. More importantly, even if a Ni_2E_2 complex has a well-characterised dichalcogenide E_2^{3-} diamond core structure, it may not be preserved during the course of the reaction, and it may be interconverted to other forms prior to the reaction. To assess and understand these intriguing aspects, in this work, we have explored dinickel dichalcogenides (Ni_2E_2) complexes $\{[Ni(L)]_2(E_2)\}^{2+}$ (E = O(**1**), S(**2**), Se(**3**) and Te(**4**)) with all four chalcogen atoms to understand the electronic structure, bonding and its implication in activating the C–H bonds of dihydroanthracene using DFT and *ab initio* calculations (CASSCF, DLPNO-CCSD(T)) methods. Using this theoretical method, we aim to answer the following intriguing questions (i) Is the nature of E (E = O, S, Se, Te) crucial in dictating the formation of specific isomers among di-, sub-, and chalcogenides in $\{Ni_2E_2\}$ complexes? (ii) how do the covalency and the corresponding electronic structure evolve as we move down the group from O to Te? and (iii) are these compounds capable of performing C–H bond activation? If so, what dictates their reactivity?

Computational details

All the geometry optimizations calculations were carried out using the Gaussian 09 suite of programs.[59] The optimisations

have been performed with B3LYP functional.[60–62] The B3LYP has a proven track record of predicting the structures and the energetics accurately for such metal-mediated catalytic reactions. LACVP basis set comprising LanL2DZ – Los Alamos effective core potential for Ni[63–65] and a 6-31G* basis set for the C, H, N, O, and S[66,67] atoms has been employed for geometry optimisation, and the optimised geometries were then used to perform single-point energy calculations using a B3LYP-D3/SDD[68] (S, Se, Te); TZVP (all) level. The solvation energies have been computed using the PCM solvation model,[68,69] employing dichloromethane as the solvent. Frequency calculations were performed on the optimised structures to verify that they are minima on the potential-energy surface (PES) and also to obtain free energy corrections. The quoted DFT energies are B3LYP-D3 solvation free energies incorporating zero-point, enthalpy, and entropic corrections at 298.15 K unless otherwise mentioned. The fragment approach available in Gaussian 09 is employed to aid smooth convergence in the case of radical intermediates. As the ligands chosen for this study favours $\{Ni^{II}{}_2(\mu\text{-}\eta^2\text{:}\eta^2\text{-}E_2)\}$ geometry, to obtain the other extreme structure *i.e.* $\{Ni^{III}{}_2(\mu\text{-}E_2)\}$ the Ni–Ni and E–E bonds are fixed to the reported X-ray structures.[27,31,51,53,58,70–73] The natural bonding orbital (NBO)[74] and the spin-natural orbital (SNO)[75,76] analysis have been performed using the Gaussian 09 suite of programs. In the molecular orbital diagram *n* represents the orbital's number.

The strain energy (ΔE_{strain}) has been calculated to obtain the destabilising steric energy associated with the transition states. The transition states are divided into two fragments, *A* (catalyst part) and *B* (substrate part) and solvent phase single-point calculations were performed on this geometries. We have estimated the energy using the following equation

$$\Delta E_{strain} = TS(A + B)(E_{solvation+Gibbs}) - A(E_{solvation+Gibbs}) - B(E_{solvation+Gibbs})$$

The ORCA 4.2 package[77] was used to calculate the absorption spectra and to perform SA-CASSCF calculations, DLPNO-CCSD(T) calculations and for calculating non adiabatic coupling of the transition state. Time-dependent density functional theory (TDDFT) implemented in the ORCA program was used for the calculation of excitation energies. To obtain these electronic transitions for all the four complexes ^{1}**1–4**$_{(t,t)}$, the time-dependent (TD) DFT method has been used. For complexes **1–3**, TDDFT calculations have been performed by using B3LYP functional along with the def2-TZVP basis[78] set for all atoms and def2TZVPP basis set for complex **4** considering the presence of heavier Te atoms.[79] The RIJCOSX approximation with def2/J auxiliary basis set has been employed. Further, the domain-based local pair natural orbital approximation to coupled-cluster theory with single, double, and perturbative triple excitations, DLPNO-CCSD(T)/cc-PVTZ method has been employed to gain confidence on the spin-state energetics.[80–83] The zero-field splitting (ZFS) parameters were estimated by utilising state-average complete active space self-consistent field (SA-CASSCF) theory[84,85] along with the incorporation of N-Electron Valence State Perturbation Theory (NEVPT2).[86,87] The CASSCF/NEVPT2 calculations use a combination of basis set DKH-def2-TZVP[88] for Ni, O, S, and Se,[89] Sapporo-TZP-2012 for Te.[90] The CASSCF calculations have been performed with active space CAS(16,10) and CAS(20,12), including 10 orbitals of two nickels for the former and two orbitals of chalcogenides in the later one active space and performed calculations only considering five singlets, triplets, and quintets states (CASCI calculation conducted to assess low-lying multiplets and have chosen all the states which like within the energy window of ~4000 cm^{-1}. This has been consistently kept for all complexes. Other excited states were found to lie much higher in energy, and hence, we have chosen to include five singlets, 5 triplets and 5 quintets). We employed a time-dependent response approach to calculate the non-adiabatic coupling (NAC) parameters of the transition state. For this analysis, we have used the def2-TZVP basis set for O, S, and Se atoms along with Ni metal center, and the Sapporo-TZP-2012 basis set for the Te atom.

The *J* values were computed from the energy differences between the high spin (EHS) state and the low spin (EBS) state determined using the broken symmetry (BS) approach developed by Noodleman.[91,92] Negative and positive values for *J* correspond to antiferromagnetic and ferromagnetic interactions, respectively. The following notation $^{M}X_{(sNi1,sNi2)}$ where superscript 'M' denotes the total multiplicities of the spin-coupled dimer and subscript '(sNi1, sNi2)' denotes the spin multiplicity on Ni(1) and Ni(2) atoms are employed throughout the report. MO diagram were generated using the G09 suite.

Results and discussion

Electronic structure and bonding of complex 1–4

We have performed DFT calculations on all the four dinickel dichalcogenide (Ni_2E_2) complexes (where E = O, S, Se, Te) supported by 1,4,7,10-tetramethyl-1,4,7,10-tetraazacyclododecane ligand, considering all possible spin states arising due to d^8 electronic configuration for both the nickel–metal centre, *i.e.* Ni centres can possess $S = 0$ and $S = 1$ state and could be coupled ferro/antiferromagnetically in the latter. In all four complexes, the $S_T = 0$ state that arises from the antiferromagnetic coupling between two Ni^{II} centres $S = 1$ state is found to be the ground state (^{1}**1–4**$_{(t,t)}$). This is followed by the corresponding ferromagnetically coupled state (^{5}**1–4**$_{(t,t)}$) at 12.3 kJ mol^{-1}, 16.1 kJ mol^{-1}, 12.4 kJ mol^{-1}, and 71.5 kJ mol^{-1}, for **1–4**, respectively. The singlet state, on the other hand, is found to be at 336.5 kJ mol^{-1}, 156.4 kJ mol^{-1}, 159.8 kJ mol^{-1}, and 152.3 kJ mol^{-1} for complexes **1–4**. The states with $S = 0$ spin on either one of the Ni^{II} centres (^{3}**1–4**$_{(t,s)}$) or both the Ni^{II} centres (^{1}**1–4**$_{(s,s)}$) were found to lie much higher in energy. The singlet-quintet gap ($\Delta E(^1\mathbf{1}_{(t,t)}{-}^5\mathbf{1}_{(t,t)})$) is found to be the smallest for **1**, followed by **3**, **2**, and **4**, which has a very large gap (≈72.0 kJ mol^{-1}) (see Fig. S1–S17‡). A close analysis reveals that while the geometry is maintained as $[Ni^{II}{}_2(\mu\text{-}\eta^2\text{:}\eta^2\text{-}E_2)(L)_2]^{2+}$ both at the singlet and quintet state for all complexes with the exception of quintet state at **4**. The singlet state is the ground state for complex **4**, whereas the quintet excited state adopts a *trans*-endon E_2 geometry, leading to a substantially larger

energy gap compared to other states. Our AIM analysis further confirms that the quintet state of complex **4** features only one Ni–Te bond (see ESI, Fig. S15‡ for details). Further, to obtain confidence in this spin-state ordering, we have also performed DLPNO-CCSD(T)[81–83] calculations on the DFT optimised geometries, and this method also predicts the $S_T = 0$ as the ground state (see Tables S1 and S2‡), though the ground state-excited state gap is lower compared to DFT methods.

The optimised structures of all possible states and the spin density plots are given in Fig. 1 (see ESI Fig. S1–S17‡ for optimised geometries and spin density plots). The ground-state structure of all four complexes has a centre of symmetry maintained with all four Ni–E bond lengths being nearly equal (E = O 2.048 Å, *S* = 2.595 Å, Se = 2.699 Å, and Te = 2.885 Å). The E–E bond distances in $^1\mathbf{1}_{(t,t)}$ and $^1\mathbf{2}_{(t,t)}$ are found to be shorter than that observed in earlier reported $\{Ni_2^{III}E_2\}/\{Ni_2^{II}(\mu\text{-}\eta^2\text{:}\eta^2\text{-}E_2)\}$ complexes (E = O 1.500 Å; *S* = 2.335 Å) but in case of complex $^1\mathbf{3}_{(t,t)}$ and $^1\mathbf{4}_{(t,t)}$, it is larger than the reported complexes (E = Se = 2.503 Å and Te = 2.823 Å). At the same time, the Ni–Ni bond distance is found to be longer than the previously reported complexes.[43] However, the Ni–E–Ni and E–Ni–E bond angles for $^1\mathbf{2}$–$\mathbf{4}_{(t,t)}$ match well with the previous literature reports (see Table S3‡). The energies computed for two isomeric bis(μ-oxo) $\{Ni_2^{III}E_2\}$ and side-on $\mu\text{-}\eta^2\text{:}\eta^2$-peroxo$[Ni^{II}_2(\mu\text{-}\eta^2\text{:}\eta^2\text{-}E_2)(L)_2]^{2+}$ forms reveals that the side-on isomer is more stable for all four species **1**–**4** with the energy margin of 60–144 kJ mol^{-1} (see Table S2, Fig. 2, and S18‡). The WB index (Wiberg Bond Index) computed reveals an increase in the Ni–E bond index and a decrease in the E–E bond index as we move from **1** to **4** (see Tables 1 and S4‡). As these two parameters are correlated to the nature of the two isomeric forms, it is clear that as we move from **1** to **4**, the geometries tend to have a stronger side-on $\mu\text{-}\eta^2\text{:}\eta^2$-peroxo character. So based on the data of previously reported dichalcogenide complexes, it can be seen that chalcogenide complexes $^1\mathbf{1}$–$\mathbf{4}_{(t,t)}$, $^1\mathbf{1}_{(t,t)}$, and $^1\mathbf{2}_{(t,t)}$ fall into the dichalcogenide category. While complex $^1\mathbf{3}_{(t,t)}$ falls between the selenide and subselenide categories, which confers E_2 exists as E_2^{2-} ($\mu\text{-}\eta^2\text{:-}\eta^2$peroxo) dinickel(II) complex.

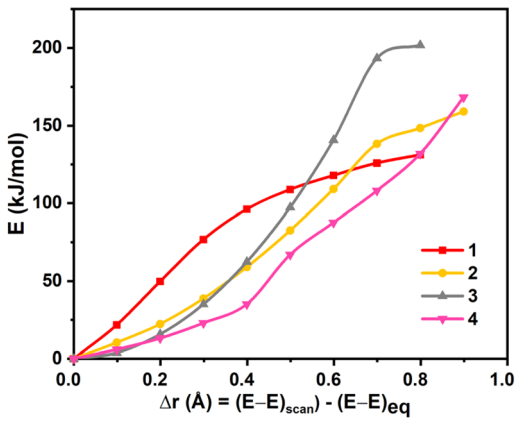

Fig. 2 Rigid scan performed by varying the E···E distance in complexes **1**–**4**. The *x*-axis represents variation in the E···E distance with respect to the equilibrium geometry.

The computed spin state for the ground state reveals strong delocalisation of spin density to the coordinated atoms, and at the antiferromagnetic state, the bridging atoms E has a net spin density of zero, and this is due to equal spin delocalisation of positive and negative spin densities (∼0.07) from Ni(1) and Ni(2) centers. The spin density on the metal center decreases as we move from **1** to **4**, suggesting strong delocalisation of spin density to the coordinated atoms. This indicates a stronger covalency for the Ni–E bond as we move down the group. To further validate this point, atoms-in-molecule (AIM) calculations were performed. These calculations reveal $|V(r)/G(r)|$ ratio of 0.91, 1.05, 1.10 and 1.20 for **1**–**4**, respectively (see Table 1 and Fig. S19–S22‡). This reveals that the Ni–O bond is strongly ionic while Ni–S, Ni–Se, and Ni–Te fall in the borderline cases with increasing per cent of covalency as we move down the group. The NBO analysis also affirms this point (see Fig. S23–S27‡). Further, NBO second-order perturbation theory donor–acceptor interactions also reveal an increase in donation from E to Ni orbitals as we move down from O to Te with the stabilisation energy of 13.8, 19.4, 22.4, and 23.0 kJ mol^{-1}, respectively. The reason for greater stabilisation is routed back to the enhanced p-character of the sp hybrid orbital of the Ni involved in the interaction as we go down in the series. This is also accompanied by a concomitant reduction of p-character (or increase in s-character for alpha spin-up orbitals see Fig. S27 and Table S5‡) of the donor orbital of E as we move down the group.

The Eigen-value plot corresponding to the d-orbitals of **1**–**4** is shown in Fig. S28–S31.‡ As expected, the Ni^{II} centre has $(d_{xy})^2(d_{yz})^2(d_{xz})^2(d_{z^2})^1(d_{x^2-y^2})^1$ electronic configuration. However, the order of the d-orbitals is drastically different if we compare **1** with **2**–**4**. Particularly a very strong $\pi_{Ni(d_{yz})\text{–}O(p_y)}$ overlap can be seen in the case of complex **1**, and a strong $\sigma_{Ni(d_{xy})\text{–}E(p_x)}$ can be seen in complexes **2**–**4**, and these two different interactions are leading to the stabilisation of d_{yz} and d_{xy} as the lowest-lying orbitals for **1** and **2**–**4** complexes, respectively. The SA-CASSCF(16,10) and SA-CASSCF(20,12) calculations were performed to ascertain the nature of the ground state electronic configuration. The first set includes the Ni^{II} orbitals of both metal centres, and the second set includes two orbitals of the E_2 moiety, and both calculations reveal the ground state with multiplicity 1 configuration shows very little mixing of the excited states (see Table S6 and Fig. S32–S39‡). The calculations suggest that all four complexes, from O to Te, exhibit a ground state predominantly characterized by one configuration $(d_{xz}^2d_{yz}^2d_{xy}^2d_{yz}^2d_{xz}^2d_{xy}^2d_{x^2-y^2}^1d_{z^2}^1d_{z^2}^1d_{x^2-y^2}^1)$, with a contribution of 88.9%–94.3%, and minor mixing with the first excited state, contributing 3.3–7.1%, alongside very little contributions from other higher excited states. The magnetic coupling is estimated using the ground state structure, employing the standard protocol, and this yields the *J* value is −303.0 cm^{-1}, −343.7 cm^{-1}, −354.2 cm^{-1}, and −422.0 cm^{-1} for complexes **1**–**4**, respectively. These values suggest a strong antiferromagnetic coupling between two nickel(II) centres (see Table 1), with the magnitude of coupling increasing as we move down the group. The antiferromagnetic coupling results from the strong overlap between the $d_{x^2-y^2}$ orbitals on the Ni^{II} centres (nb^*_{3g}, where $n = 4$ for complex **1**, $n = 2$ for complex **2** and **3**, and $n = 3$ for complex

Table 1 DFT computed J_s, WB indices, absorption features, $|V(r)/G(r)|$ ratio of Ni1–E1 bond from AIM for the ground state geometry, and computed barrier height for hydrogen atom abstraction in complexes **1–4**

Complexes	J (in cm^{-1})	WBI			λ_{max} (nm)	$\lvert V(r)/G(r)\rvert$	ν(E–E) (cm^{-1})	ΔG(C–H) (kJ mol^{-1})
		Ni_1–E_1	Ni_2–E_1	E_1–E_2				
$^1\mathbf{1}_{(t,t)}$	$S = 0$ (AF, −303)	0.261	0.261	1.032	288, 315, 377, 560 (386, 450)	0.91	829.7	58.5
$^1\mathbf{2}_{(t,t)}$	$S = 0$ (AF, −344)	0.363	0.363	1.013	286, 327, 411, 580 (320, 394, 464)	1.05	421.2	68.2
$^1\mathbf{3}_{(t,t)}$	$S = 0$ (AF, −354)	0.376	0.376	0.922	281, 380, 449, 580 (390, 410, 690)	1.10	268.4	89.3
$^1\mathbf{4}_{(t,t)}$	$S = 0$ (AF, −422)	0.478	0.478	0.932	299, 333, 413, 506 (314, 420, 487)	1.20	173.1	95.4

4), and this overlap tend to get stronger as we go down from O to Te. This strong antiferromagnetic nature is important during the electron transfer process from the substrate to the oxygen centric Ni–E π* orbital. This is reflected in the nature of computed SOMO (see Tables 1 and S7‡). As we move down the group, the enhancement in antiferromagnetic coupling was noticed earlier in several other examples reported.[93] Although direct experimental evidence for the antiferromagnetic coupling is absent, room temperature effective magnetic moment measured for **3** is found to be 2.71 μ_B. This value is significantly smaller than the expected value for the $S_T = 2$ ferromagnetically coupled state and suggests that the ground state is $S_T = 0$ with some per cent of the $S = 2$ population at room temperature, placing the exchange coupling in the range of ∼200–300 cm^{-1}.[58]

To further understand the nature of bonding, qualitative MO diagrams based on the computed ground state are constructed for complexes **1–4** [53] (see Fig. 3 for complex **3** and Fig. S40–S43‡ for complexes **1**, **2**, and **4**, respectively). These were constructed assuming a pseudo D_{2h} symmetry for the $\{Ni_2E_2N_8\}$ core and quantification of the deviation reveal that except in case of complex **1** where the deviations are relatively larger, it lies in the range of 0.11 to 0.22 (Fig. S40‡). For all four complexes, $n\mathrm{b}_{1g}$ (where $n = 1$ for complex **1**, and $n = 2$ for complex **2–4**), which is a combination of $\pi^*(E_1(p_y) - E_2(p_y))$ and $\delta(Ni_1(d_{yz}) - Ni_2(d_{yz}))$ orbitals, is found to be the highest occupied molecular orbital (HOMO). For dichalcogenide complexes, the b_{1g} is expected to have a significant $\delta(Ni_1(d_{yz}) - Ni_2(d_{yz}))$ contribution and very little/no $\pi^*(E_1(p_y) - E_2(p_y))$ contribution. For subchalcogenide complexes, the contribution is expected to be significant in $\pi^*(E_1(p_y) - E_2(p_y))$ orbital with a sizeable $\delta(Ni_1(d_{yz}) - Ni_2(d_{yz}))$ orbital contribution. For chalcogenide, on the other hand, as one more electron from the Ni centre is lost, both $\pi^*(E_1(p_y) - E_2(p_y))$ and $\sigma^*(E_1(p_z) - E_2(p_z))$ will be occupied with very little/no contributions from Ni centres. From the qualitative MO diagram, it is clear that complex **1** falls in the dichalcogenide category while complexes **2–4** have a strong subchalcogenide character, which is found to be increasing as we move down the group. Further, the lowest unoccupied orbitals (LUMO) in complexes **2–4** were found to have a strong $Ni(d_{x^2-y^2})$ character along with the E_2 character suggesting loss of one electron as expected for subchalcogenide. As this orbital is important for its reactivity towards C–H bond activation, a strong metallic character detected for **2–4** is likely to help reduce the kinetic barrier (*vide infra*).

As the qualitative MO diagram developed[53] can be correlated directly to the experimental absorption features, we used time-dependent density functional theory (TD-DFT) to compute absorption features of **1–4** (see Table 1 and Fig. S44‡) for the ground state geometries. The major absorption features observed in experiments for complex **3** are reproduced in our calculations, particularly a peak at 281 nm observed corresponds to metal-to-ligand charge transfer ($1b_{3g}$ to $2b^*_{3g}$ in Fig. 3), while the peaks at 380 nm ($1b_{2u}$ to $2b^*_{2u}$ in Fig. 3) and 449 nm ($1b_{2u}$ to $2b^*_{3g}$ in Fig. 3) are considered as bonding orbitals of Ni_2Se_2 to pure antibonding orbitals of Se_2^{2-}. The peak at 580 nm (a_g to $3b_{1u}$ in Fig. 3) shows ligand-to-metal charge transfer. The $1b_{2u}$ to nb^*_{3g} (where $n = 4$ for complex **1**, $n = 2$ for complex **2** and **3**, and $n = 3$ for complex **4**) transition is observed in all four complexes, with the energy gap decreasing, we move from oxygen to Te (315 nm, 411 nm, 449 nm, and 506 nm for **1–4**, respectively). This is consistent with the decrease in the E–E bond order observed as we move from **1–4**. Further, the computed spectra for complexes **2** and **4** also qualitatively agree with earlier reported complexes having different terminal ligands.[53] The calculations performed reproduce the experimental observables offering confidence in the methodology employed.

Reactivity of complexes 1–4 towards C–H activation

Riordan and co-workers reported that diselenide dinickel complex exhibited reactivity towards 9,10-dihydroanthracene (DHA) and cyclohexadiene (CHD) molecules.[58] The mechanism adapted for the C–H bond activation (Scheme S1‡) reveals that the chalcogenide atom (*via* **ts1**) activates the C–H bond, leading the Ni–E_1–H intermediate (**Int1**) with the second hydrogen atom abstraction *via* **ts2** by chalcogenide atom E_2 leading to two hydrochalcogenide Ni^{II} product (**PC**) that was detected by experiments and characterised using X-ray and spectral methods.[58]

The computed potential energy surface for **1–4** is shown in Fig. 4 and S45.‡ For complexes **1**, **3** and **4**, the triplet state (^{5}**1,3-4**$_{ts1(t,t)}$) has the lowest barrier of 58.5, 89.3 and 95.4 kJ mol^{-1}, respectively. For complex **2**, on the other hand, the singlet state ($^1\mathbf{2}_{ts1(t,t)}$) was found to have the lowest barrier of 68.2 kJ mol^{-1}. The ^{1}**1,3-4**$_{ts1(t,t)}$ and $^5\mathbf{2}_{ts1(t,t)}$ transition states were found to lie at 78.5, 99.8, 97.7 and 82.0 kJ mol higher. For complex **3**, the computed barrier height of 89.3 kJ mol^{-1} is slightly higher than expected for an otherwise facile C–H bond activation pathway, and this larger barrier, however consistent with the

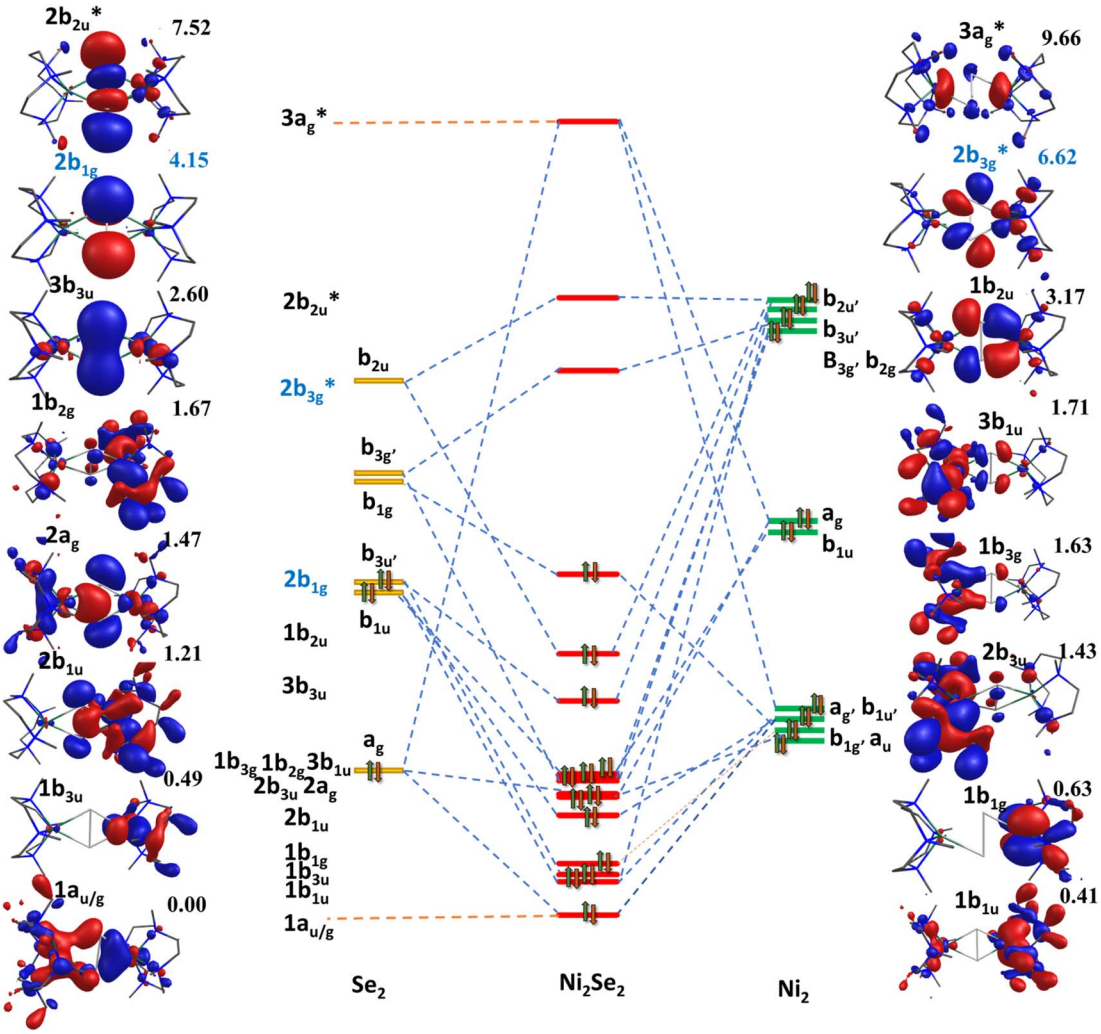

Fig. 3 Qualitative molecular orbital diagram for complex **3** (energy in eV). Here HOMO–LUMO energy written in blue color code.

experimental finding that the reaction does not proceed at ambient temperature and temperature as high as 55 °C is required to effect this transformation.[94] We have also estimated the barrier height at the singlet surface for complex **3** (^{1}**3**$_{ts1(s,s)}$) to assess and analyse, if the closed-shell singlet participate at all in the reactivity. This set of calculations resulted in a prohibitively high barrier height of 302.0 kJ mol^{-1}, thereby ruling out the possibility of this state contributing to the reactivity, as depicted in Fig. 4c.

In all the transition state computed, hydrogen atom abstraction is detected, leading to a carbon-centred radical, as also evidenced by IRC analysis (See Fig. S46 and S47 in ESI‡). In all the transition states computed, the ∠E–H–C bond angle was found to be lying in the range of 154°–172° suggesting σ-pathway for the H atom abstraction. This is also attributed to the nature of the LUMO orbitals at the reactant, which has significant p_x/p_y orbitals of the E atom contribution along with $d_{x^2-y^2}$ orbital of the Ni^{II}, promoting the σ-pathway. At the transition state, electron transfer is nearly complete, with the early transition state for **1** and the late transition state for **2–4**, reflecting the difference in the electronic structure described earlier (dichalcogenide *vs.* subchalcogenide). As dichalcogenide complexes are expected to have lower pK_a than subchalcogenide complexes, the variation in the transition state observed correlates well with the established electronic structure. Further, the HAT abstraction is accompanied by the electron transfer due to which the E_1–E_2 bond is fully broken in all the complexes **1–4** with a significant radical character generated on $E_2^{\bullet}$. This radical character, in turn, leads to partial Ni = E_2 character and the formation of a weakly interacting monomeric Ni hydrochalcogenide product (see Fig. S2‡). This also suggests significant electronic cooperativity between two Ni centres, rationalising the reason for the higher reactivity of dinickel dichalcogenide complexes compared to their monomeric analogues (see Table S8‡).

The computed barrier height reveals the following order of reactivity **1** > **2** > **3** > **4**, suggesting higher reactivity of O, which has a dichalcogenide character (also very high basicity of –O center) and lower reactivity for subchalcogenide complexes. As the degree of subchalcogenide increases, as we move from **2** to **4**, the barrier height also increases proportionately, suggesting much lower reactivity for subchalcogenide complexes (see Fig. 4

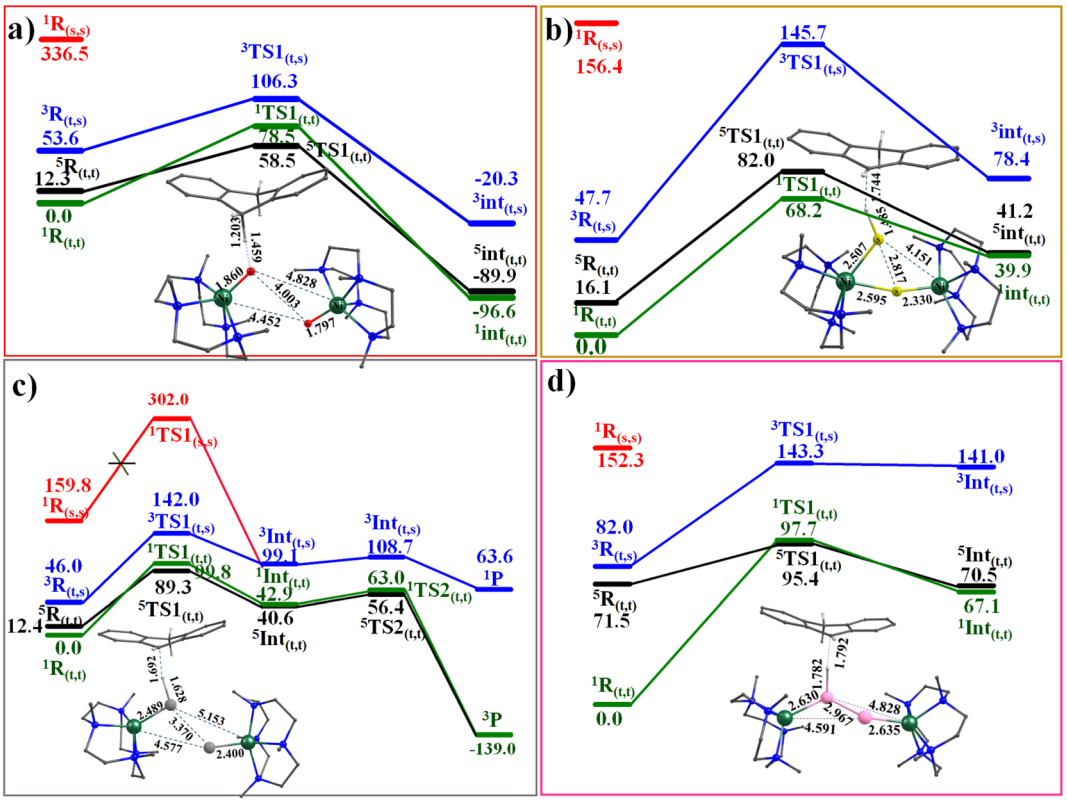

Fig. 4 Computed potential energy surface energy surface for the C–H activation by complexes (a) **1**, (b) **2**, (c) **3**, and (d) **4**.

and 5). To understand the trend in the estimated barrier height, the strain energy analysis of the transition state was performed, which reveals that the catalyst strain is significant, and this is compensated to some extent by a favourable strain energy for the substrate for all four complexes. A larger strain in the catalysts was reflected as we moved from **1** to **4**, which is directly related to the computed barrier height. The interaction energy computed reveals a favourable overlap of the frontier orbitals as expected, and this interaction energy was found to diminish as we move from **1** to **4** leading to a larger barrier height. Thus increase in the barrier height observed as we move from **1** to **4** originates from both larger strain and smaller interaction energy (see Table S9‡).

In the next step, we would like to extend the HAT event further and quantify it in detail by exploring the non-adiabaticity of the first hydrogen abstraction transition state (**ts1**) for all four complexes (**1–4**). In this connection, it is important to highlight the seminal work performed by Hammes-Schiffer and co-workers that describes the vibronic nonadiabaticity between the electron–proton quantum subsystem and the classical nuclei, along with the electron–proton nonadiabaticity within the electrons and proton(s) of the quantum subsystem for an enzyme that supported the use of Golden rule rate constant expression.[95–101] While this approach is the best suited to analyse our transition state, the gap computed between different multiplets at the transition state in our case was too small to develop the full potential energy surface (>2 kJ mol^{-1} for **1**). We then turn to calculate the non-adiabatic coupling (NAC) of the first hydrogen abstraction using a time-dependent response approach, which avoids the explicit computation of excited-state wave functions.[102] These calculations were performed using the ORCA suite (see Computational details). These calculations reveal that as we move from **1** to **4**, there is a decrease in the maximum non-adiabatic coupling strength (see Table S10‡). This observation suggests that complexes **1** and **2** possess larger non-adiabatic coupling, and **3** and **4** have relatively smaller values, clubbing the Se and Te together in this context (see Table S10‡). To further understand the nature of the hydrogen atom transfer (HAT) reaction, we have further expanded our analysis and performed spin-natural orbital analysis for all four complexes **1–4**. For **1**, the carbon atom of the substrate exhibits a small spin density of approximately −0.19. This, combined with the SNO analysis, indicates that the dominant proton transfer pathway is likely operational. Conversely, in complex **2**, only a dominant HAT nature is evident, with the occupation value of 0.69e of the spin natural orbital, as supported by the spin density plot displaying a significant electron density of −0.46 at the carbon radical centre of the DHA molecule. In the cases of complexes **3** and **4**, a pronounced radical nature is also observed at the carbon center, with values of −0.48 and 0.44, respectively, and the SNO analysis reveals that complex **3** exhibits a strong PCET character (1.00e) with a slight HAT character (0.84e), while in complex **4**, a strong HAT character (1.00e) is predominant in the transition state, albeit with a slight PCET character. The computed data indicate a trend: as we progress from

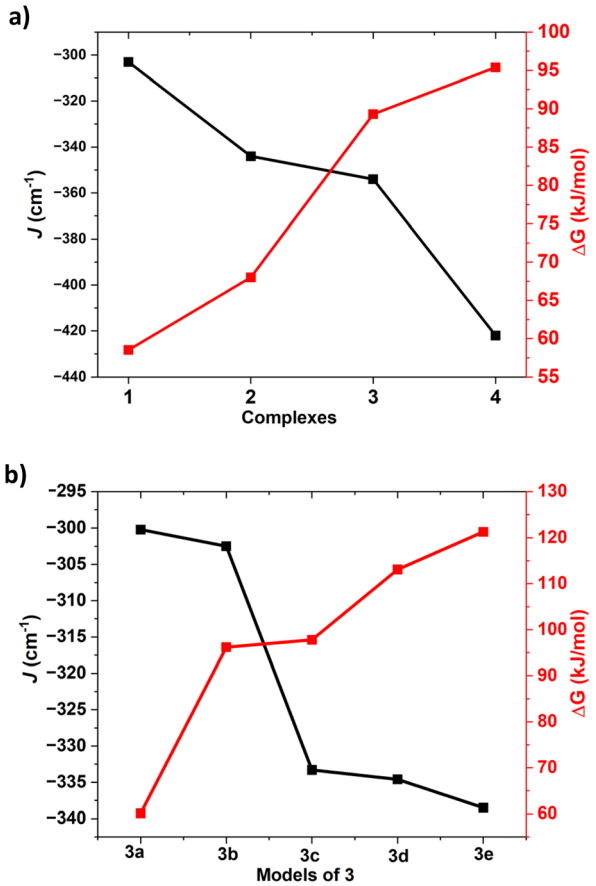

Fig. 5 (a) First hydrogen abstraction barrier height correlation with J value of complexes **1–4** (b) magneto–structural correlation for the substituted geometries of the complex **3** (**3a–3e**).

complex **2** to **4**, the HAT nature of the transition state becomes increasingly prominent, and this is also in line with the increase in the metal–ligand covalency that is expected to promote HAT pathway (see Fig. S48–S52 and S53–S56‡ for EVP).[103] After the hydrogen atom abstraction, the formation of radical intermediate (**Int1**) is exothermic for **1** and endothermic for the rest (−96.6, 39.9, 40.6 and 67.1 kJ mol^{-1}, for **1–4**, respectively) with $S_T = 0$ ground state arising from antiferromagnetic for all with the exception of **3** (here $S_T = 2$). In all cases, the corresponding exchange coupled excited state was found to lie close within an energy margin of 1.3–6.6 kJ mol^{-1}, with the triplet states lying much higher in energy (38–71 kJ mol^{-1}). At this species, the E–E bond is found to be broken in all cases with a concomitant strengthing of the Ni–E bonds. The chalcogenide that abstracts the H atom also creates a Ni–E bond shorter than that of the reactant.

In **3**, the Ni–Se bond distance is found to be 2.395 Å, and this is in excellent agreement with the value reported from the X-ray structure (2.389 Å), offering further confidence in the chosen methodology.[58] Encouraged by the direct experimental evidence that is available for the intermediate computed with species **3**, we also extended our mechanism to probe the barrier for the second hydrogen atom abstraction. This is presumed to route through the transition state (**ts2**; see Fig. 4) with a barrier for 15.8 kJ mol^{-1} from the intermediate, suggesting a facile abstraction of the second hydrogen atom leading to the formation of anthracene by −139.0 kJ mol^{-1} gain in energy.

The results obtained from DFT calculations exhibit a noteworthy trend in the structural and bonding analysis of complexes **1–4**. In all four complexes, the high spin antiferromagnetic state ^{1}**1–4**$_{(t,t)}$ is identified as the ground state, and this is due to the strong overlap of $d_{x^2-y^2}$ orbitals of two Ni centres. The nature of the ground state is further affirmed by the SA-CASSCF and DLPNO-CCSD(T) methods. Further AIM analysis reveals an increase in Ni–E bond covalency as we move down the group by 15.0%, 20.9% 31.9% for Ni–S, Ni–Se and Ni–Te, respectively, compared to the Ni–O bond. This is attributed to a stronger donation from E to Ni as we move down the group (40.5%, 62.3% and 66.7% for Ni–S, Ni–Se and Ni–Te, respectively, compared to the Ni–O bond). The increase in the Ni–E bond covalency was also found to enhance the multi-configurational mixing of states in SA-CASSCF calculations suggesting multistate reactivity for higher analogues.[41]

The singlet state arising from the $S = 0$ state (^{1}**1–4**$_{(s,s)}$) at each Ni centres is too high in energy with respect to the transition state computed at the singlet and triplet surfaces and hence rules out the possibility of these states involvement in the HAT reaction. Further, the triplet state ^{3}**1–4**$_{(t,s)}$ is also found to be higher in energy compared to a quintet and singlet state arising from antiferromagnetic coupling and hence is unlikely to participate in the HAT reaction invoking two-state reactivity or TSR scenario for the HAT reactions. The C–H bond activation for all four species was found to be either routed *via* $S = 2$ states (for **1**, **2**, and **4**) or *via* close-lying $S = 0$ states facilitating two-state reactivity (in case of **3**). In all four cases, partially closed-shell triplet states (*i.e.*, a triplet on one Ni center and a singlet state on the other) and fully closed-shell singlets ($S = 0$ on both Ni centers) were found to be high in energy, with transition states prohibitively high to participate in the reaction. This suggests that only the spin-coupled triplet states of the Ni centers contribute to the reactivity.

All these calculations suggests that the quintet-singlet gap that is correlated to the exchange interaction between two Ni centres is key to the reactivity. As this parameter is correlated to the exchange interaction, we have plotted the computed J values for these complexes along with the rate-determining step barrier height corresponding to the C–H bond activation (Fig. 5).

This suggests that there is a clear correlation as the J value is found to increase in the order **1** < **2** < **3** < **4** with the increase in the quintet-singlet gap while the reactivity follows the reverse trend (**1** > **2** > **3** > **4**), suggesting greater reactivity when the antiferromagnetic coupling between the two centres are weak/small.[104,105] Deeper orbital analysis and overlap integral computed suggest strong antiferromagnetic coupling is found to associated with the greater $d_{x^2-y^2}|p_x|d_{x^2-y^2}$ overlap, which is important during the electron transfer process from the substrate to the chalcogenide centric Ni–E(π^*) orbital. The quintet state of complex **1** having strong Ni-centric HOMO and LUMO due to its dichalcogenide and stronger Ni(II) character

enable the facile transfer of α-electron from the C–H bond maximising the exchange-enhanced reactivity,[106] stabilising the corresponding transition state. Further, as the α-electron, which is getting transferred from the substrate, triggers Ni–E bond cleavage, the transferred electron is found to be located on the E(2) centre, resulting in the formation of Ni(II)–E$^{\bullet}$ species at the transition state. As the coupling between Ni(II) and E$^{\bullet}$ has to be ferromagnetic due to orbital orthogonality (see Table S11 in ESI‡ for computed J_s), this quintet state is the preferred transition state. In the singlet state, as shown in the orbital evolution diagram, the Ni(II)–E(2)$^{\bullet}$ forced to be in antiferromagnetic state (See Fig. S57 and also corresponding spin density plots in Fig. S2 and S5, S8, S11 and S16‡).

Also the careful analysis of all optimized ground state transition state geometries suggested that in the case of complex **2**, the $\{Ni_2S_2\}$ core does not break completely during the transition state formation. This observation suggests that the overlapping of sulphur 3p orbitals with the metal 3d orbitals (specifically $d_{x^2-y^2}|p_x|d_{x^2-y^2}$ overlap) persists, thereby stabilizing the antiferromagnetic state. Also, the comparison of Ni–E bond lengths was observed in complexes **1**, **3**, and **4** (ranging from 4.450 to 4.560 Å), while in the case of complex **2**, the Ni–E bond seemed significantly shorter by 2.595 Å. This shorter bond length favours antiferromagnetic coupling state as the ground state of complex **2**, in contrast to other complexes.

As we move down in the group, increased covalency and transition to subchalcogenide offer a strongly delocalised LUMO that is less electrophilic, enhancing the overall kinetic barrier. For complex **4**, a β-electron transfer from the C–H bond is noticed, enhancing the barrier height further. The pronounced electronic cooperativity at play during the C–H bond activation step is clearly discernible across complexes **1–4**. This is evidenced by the electron transfer from the C–H bond, which ultimately resides on E_2, a participant not directly engaged in the reaction. Overall, our study suggests that a ferromagnetic Ni_2E_2 would be more reactive, and if the antiferromagnetic interaction is diminished, this would also be expected to enhance the reactivity. As the antiferromagnetic interaction between the two Ni(II) centres is correlated to the Ni–E–Ni angle,[107] this offers a viable route to enhance the reactivity of higher analogues that are generally unreactive.

To further probe the correlation between the antiferromagnetic coupling and the barrier height, we have now expanded the calculations on complex **3** with various substitutes at the ligand moiety and carved out five additional models (the $-NCH_3$ group was replaced by a –NH groups, see Fig. S58 in ESI‡ for models developed; models **3a–3e**) to develop magneto–structural correlation (see Fig. 5 and S58‡). Using these models, we have computed the J and also computed the corresponding barrier height for these models. For these models, the computed exchange coupling is found to be antiferromagnetic, but the magnitude of the J was found to vary from 300.2 cm^{-1} to 338.5 cm^{-1}. The barrier height corresponding to the HAT reaction for models **3a–3e** was found to vary from 60.1 to 121.3 kJ mol^{-1} (see Table S12 in ESI‡). We have now plotted this magneto–structural correlation that connects J with the barrier height within this model series (see Fig. 5). The computed values revealed a correlation: as the antiferromagnetic coupling exchange J value increases, so does the barrier height. This supports the observed trend among complexes **1–4**, where an increase in antiferromagnetic coupling corresponds to higher barrier heights. This explains why complex **1** exhibited the highest reactivity with the lowest antiferromagnetic exchange value. This finding aligns with the observed trend of all four complexes **1–4**, where higher J values correspond to lower reactivity of the reaction (see Fig. S58 and Table S12,‡ also see Tables S13–S27‡ for detailed structural parameters).

Conclusions

Dinickel dichalcogenide complexes are important due to their diverse applications, including catalysis, electron transfer processes, magnetic properties, materials science contributions, theoretical insights, and energy conversion potential. In this study, we employed an array of theoretical tools to study in detail the structure, bonding and reactivity of a series of $\{[Ni(L)]_2(E_2)\}(PF_6)_2$ (E = O, S, Se and Te) complexes. The following conclusions are derived from our work (i) by studying the geometry, bonding and spectral features of the four dinickel dichalcogenide complexes, our calculations unambiguously suggest $\{Ni_2O_2\}$ and $\{Ni_2S_2\}$ fall under the category of dichalcogenide type complexes, while complexes $\{Ni_2Se_2\}$ and $\{Ni_2Te_2\}$ exhibits tendencies towards the subchalcogenide category. None of the complexes were found to have pure chalcogenide characters at their ground state. The geometry and spectral features are broadly in agreement with the experimental findings. (ii) The bonding Ni–E (E = O, S, Se and Te) bond is found to be ionic for O with a significant increase in covalency as we move down the group. This is associated with the greater overlap of Ni-3d orbitals with the diffused 3p/4p/5p orbitals compared to the oxygen 2p orbitals. A strong covalency also enhances the multiconfigurational character of the heavier analogues, completing the simple picture often derived from DFT. The observed covalency correlates with reactivity, as stronger covalent compounds exhibit slower reaction rates, while non-adiabatic coupling diminishes along this route, favoring hydrogen atom transfer as we progress down the series. (iii) All complexes studied have singlet ground states resulting from the antiferromagnetic coupling between two Ni centres. The C–H bond activation studies on these complexes reveal that the following order of decreasing reactivity $\{Ni_2O_2\} > \{Ni_2S_2\} > \{Ni_2Se_2\} > \{Ni_2Te_2\}$. The transition state is characterised in all cases to be a chalcogenide category, suggesting how subtle different classifications are when it comes to reactivity. Particularly during the C–H bond activation, strong electronic cooperativity between the metal centres is noticed along with variation in their classification as the E–H bond formation takes place. Investigating the multi-state reactivity of all complexes reveals that only the spin-coupled triplet states, which yield overall singlet and triplet states, dictate the overall reactivity, while the closed-shell singlets are too high in energy and do not participate in the reaction. This highlights the importance of maintaining a weak/moderate ligand field around the Ni center to achieve greater reactivity. (iv) Further, a strong correlation

between the J values and the C–H bond activation step is detected with a lower gap yielding higher reactivity. As quintet state, in general, found to have lower barriers, efforts to obtain a ferromagnetic coupling in Se or Te analogues would be fruitful in enhancing their reactivity.

Data availability

All relevant computational data associated with our study, including Cartesian coordinates, geometry, spin density plots, and detailed structural information, are available in the ESI† provided with our submission.

Author contributions

Sunita Sharma: conducted the majority of the computational studies, analysed data, and contributed significantly to the writing of the manuscript. Bhawana Pandey: assisted with computational work, data analysis, and contributed to the interpretation of the results and preparation of the manuscript. Gopalan Rajaraman: conceived and supervised the project, provided guidance on computational methodologies, analysed data, and contributed to the writing and editing of the manuscript.

Conflicts of interest

There are no conflicts to declare.

Acknowledgements

We thank SERB (SB/SJF/2019-20/12; CRG/2022/001697) for funding. SS/BP thanks UGC for the fellowship and HPC for the computational facility.

References

1 P. A. Frey and A. D. Hegeman, *Enzymatic Reaction Mechanisms*, Oxford University Press, 2007.
2 R. H. Holm and E. I. Solomon, *Chem. Rev.*, 1996, **96**, 2237.
3 B. Meunier, G. Brudvig, J. L. Mclain, S.-i. Murahashi, V. Pecoraro, D. Riley, A. Robert, J. Rodriguez, R. Sheldon and J. Valentine, *Biomimetic Oxidations Catalyzed by Transition Metal Complexes*, World Scientific, 2000.
4 H. Sigel and A. Sigel, *Metal Ions in Biological Systems: Electron Transfer Reactions in Metalloproteins*, CRC Press, vol. 27, 1991.
5 J. T. Groves, *J. Inorg. Biochem.*, 2006, **100**, 434–447.
6 P. R. O. De Montellano, *Cytochrome P450: Structure, Mechanism, and Biochemistry*, Springer, 2005.
7 J. Hohenberger, K. Ray and K. Meyer, *Nat. Commun.*, 2012, **3**, 1–13.
8 D. F. Leto, *Biomimetic Peroxo- and Oxo-manganese Complexes: Insights into Structure and Reactivity through Kinetic, Spectroscopic, and Computational Studie*, 2014.
9 R. H. Holm, *Chem. Rev.*, 1987, **87**, 1401–1449.
10 J. P. Klinman, *Chem. Rev.*, 1996, **96**, 2541–2562.
11 E. I. Solomon, U. M. Sundaram and T. E. Machonkin, *Chem. Rev.*, 1996, **96**, 2563–2606.
12 D. Wilson, M. Fataftah, Z. Mathe, B. Mercado, S. DeBeer and P. Holland, *J. Am. Chem. Soc.*, 2024, **146**(6), 4013–4025.
13 S. W. Ragsdale, *J. Biol. Chem.*, 2009, **284**, 18571–18575.
14 A. Parkins, *Activation of Unreactive Bonds and Organic Synthesis Topics in Organometallic Chemistry*, Wiley Online Library, 2000.
15 W. Keim, *Angew. Chem., Int. Ed. Engl.*, 1990, **29**, 235–244.
16 P. M. Vignais and B. Billoud, *Chem. Rev.*, 2007, **107**, 4206–4272.
17 J. C. Fontecilla-Camps, A. Volbeda, C. Cavazza and Y. Nicolet, *Chem. Rev.*, 2007, **107**, 4273–4303.
18 B. Palenik, B. Brahamsha, F. Larimer, M. Land, L. Hauser, P. Chain, J. Lamerdin, W. Regala, E. Allen and J. McCarren, *Nature*, 2003, **424**, 1037–1042.
19 J. Wuerges, J.-W. Lee, Y.-I. Yim, H.-S. Yim, S.-O. Kang and K. D. Carugo, *Proc. Natl. Acad. Sci. U. S. A.*, 2004, **101**, 8569–8574.
20 H.-D. Youn, E.-J. Kim, J.-H. Roe, Y. C. Hah and S.-O. Kang, *Biochem. J.*, 1996, **318**, 889–896.
21 A. Messerschmidt, R. Huber, T. Poulos and K. Wieghardt, *Handbook of Metalloproteins*, John Wiley & Sons, Chichester, 2001.
22 R. P. Hausinger, *Biochemistry of Nickel*, Springer Science & Business Media, 2013.
23 S. W. Ragsdale and E. Pierce, *Biochim. Biophys. Acta – Proteins Proteom.*, 2008, **1784**, 1873–1898.
24 W. Martin and M. J. Russell, *Philos. Trans. R. Soc. Lond., B, Biol. Sci.*, 2007, **362**, 1887–1926.
25 D. M. Grove, G. Van Koten, R. Zoet, N. W. Murrall and A. J. Welch, *J. Am. Chem. Soc.*, 1983, **105**, 1379–1380.
26 J. Cho, R. Sarangi, J. Annaraj, S. Y. Kim, M. Kubo, T. Ogura, E. I. Solomon and W. Nam, *Nat. Chem.*, 2009, **1**, 568–572.
27 S. Hikichi, M. Yoshizawa, Y. Sasakura, M. Akita and Y. Moro-oka, *J. Am. Chem. Soc.*, 1998, **120**, 10567–10568.
28 K. Shiren, S. Ogo, S. Fujinami, H. Hayashi, M. Suzuki, A. Uehara, Y. Watanabe and Y. Moro-oka, *J. Am. Chem. Soc.*, 2000, **122**, 254–262.
29 B. Bag, N. Mondal, G. Rosair and S. Mitra, *Chem. Commun.*, 2000, 1729–1730.
30 S. Itoh, H. Bandoh, M. Nakagawa, S. Nagatomo, T. Kitagawa, K. D. Karlin and S. Fukuzumi, *J. Am. Chem. Soc.*, 2001, **123**, 11168–11178.
31 R. Schenker, B. S. Mandimutsira, C. G. Riordan and T. C. Brunold, *J. Am. Chem. Soc.*, 2002, **124**, 13842–13855.
32 L. Que Jr and W. B. Tolman, *Angew. Chem., Int. Ed.*, 2002, **114**, 1160–1185.
33 K. Ray, F. Heims and F. F. Pfaff, *Eur. J. Inorg. Chem.*, 2013, **2013**, 3784–3807.
34 C. Krebs, D. Galonic Fujimori, C. T. Walsh and J. M. Bollinger Jr, *Acc. Chem. Res.*, 2007, **40**, 484–492.
35 L. Que Jr, *Acc. Chem. Res.*, 2007, **40**, 493–500.
36 W. Nam, *Acc. Chem. Res.*, 2007, **40**, 522–531.
37 G. Xue, R. De Hont, E. Münck and L. Que, *Nat. Chem.*, 2010, **2**, 400–405.

38 W. J. Song, Y. O. Ryu, R. Song and W. Nam, *J. Biol. Inorg. Chem.*, 2005, **10**, 294–304.
39 K. Chen and L. Que, *J. Am. Chem. Soc.*, 2001, **123**, 6327–6337.
40 Y. Mekmouche, S. Ménage, C. Toia-Duboc, M. Fontecave, J. B. Galey, C. Lebrun and J. Pécaut, *Angew. Chem., Int. Ed.*, 2001, **40**, 949–952.
41 E. Zars, L. Gravogl, M. R. Gau, P. J. Carroll, K. Meyer and D. J. Mindiola, *Chem. Sci.*, 2023, **14**, 6770–6779.
42 O. P. Lam, F. W. Heinemann and K. Meyer, *Chem. Sci.*, 2011, **2**, 1538–1547.
43 K. Kalantar-zadeh, J. Z. Ou, T. Daeneke, M. S. Strano, M. Pumera and S. L. Gras, *Adv. Funct. Mater.*, 2015, **25**, 5086–5099.
44 B. Krebs and G. Henkel, *Angew. Chem., Int. Ed. Engl.*, 1991, **30**, 769–788.
45 T. C. Brunold, *J. Biol. Inorg. Chem.*, 2004, **9**, 533–541.
46 J. L. Craft, B. S. Mandimutsira, K. Fujita, C. G. Riordan and T. C. Brunold, *Inorg. Chem.*, 2003, **42**, 859–867.
47 A. Volbeda, M.-H. Charon, C. Piras, E. C. Hatchikian, M. Frey and J. C. Fontecilla-Camps, *Nature*, 1995, **373**, 580–587.
48 A. T. Fiedler, P. A. Bryngelson, M. J. Maroney and T. C. Brunold, *J. Am. Chem. Soc.*, 2005, **127**, 5449–5462.
49 U. Ermler, W. Grabarse, S. Shima, M. Goubeaud and R. K. Thauer, *Science*, 1997, **278**, 1457–1462.
50 K. M. Van Heuvelen, J. Cho, C. G. Riordan and T. C. Brunold, *Inorg. Chem.*, 2010, **49**, 3113–3120.
51 J. Cho, K. M. Van Heuvelen, G. P. Yap, T. C. Brunold and C. G. Riordan, *Inorg. Chem.*, 2008, **47**, 3931–3933.
52 H. Sitzmann, D. Saurenz, G. Wolmershäuser, A. Klein and R. Boese, *Organometallics*, 2001, **20**, 700–705.
53 S. A. Yao, V. Martin-Diaconescu, I. Infante, K. M. Lancaster, A. W. Götz, S. DeBeer and J. F. Berry, *J. Am. Chem. Soc.*, 2015, **137**, 4993–5011.
54 S. A. Yao, K. M. Lancaster, A. W. Götz, S. DeBeer and J. F. Berry, *Chem.–Eur. J.*, 2012, **18**, 9179–9183.
55 R. Sarangi, S. DeBeer George, D. J. Rudd, R. K. Szilagyi, X. Ribas, C. Rovira, M. Almeida, K. O. Hodgson, B. Hedman and E. I. Solomon, *J. Am. Chem. Soc.*, 2007, **129**, 2316–2326.
56 J. T. Henthorn, G. E. Cutsail III, T. Weyhermüller and S. DeBeer, *Nat. Chem.*, 2022, **14**, 328–333.
57 M. C. Marques, C. Tapia, O. Gutiérrez-Sanz, A. R. Ramos, K. L. Keller, J. D. Wall, A. L. De Lacey, P. M. Matias and I. A. Pereira, *Nat. Chem. Biol.*, 2017, **13**, 544–550.
58 J. Wallick, C. G. Riordan and G. P. Yap, *J. Am. Chem. Soc.*, 2013, **135**, 14972–14974.
59 M. Frisch, G. Trucks, H. Schlegel, G. Scuseria, M. Robb, J. Cheeseman, G. Scalmani, V. Barone, B. Mennucci and G. Petersson, Gaussian Inc, Wallingford, 2009.
60 C. Lee, W. Yang and R. G. Parr, *Phys. Rev. B: Condens. Matter Mater. Phys.*, 1988, **37**, 785.
61 M. P. Andersson and P. Uvdal, *J. Phys. Chem. A*, 2005, **109**, 2937–2941.
62 P. J. Stephens, F. J. Devlin, C. F. Chabalowski and M. J. Frisch, *J. Phys. Chem.*, 1994, **98**, 11623–11627.
63 P. J. Hay and W. R. Wadt, *J. Chem. Phys.*, 1985, **82**, 299–310.
64 P. J. Hay and W. R. Wadt, *J. Chem. Phys.*, 1985, **82**, 270–283.
65 W. R. Wadt and P. J. Hay, *J. Chem. Phys.*, 1985, **82**, 284–298.
66 A. Savin, O. Jepsen, J. Flad, O. K. Andersen, H. Preuss and H. G. von Schnering, *Angew. Chem., Int. Ed. Engl.*, 1992, **31**, 187–188.
67 W. J. Hehre, *Acc. Chem. Res.*, 1976, **9**, 399–406.
68 D. Andrae, U. Haeussermann, M. Dolg, H. Stoll and H. Preuss, *Theor. Chim. Acta*, 1990, **77**, 123–141.
69 M. Cossi, N. Rega, G. Scalmani and V. Barone, *J. Comput. Chem.*, 2003, **24**, 669–681.
70 M. T. Kieber-Emmons and C. G. Riordan, *Acc. Chem. Res.*, 2007, **40**, 618–625.
71 C. Mealli and S. Midollini, *Inorg. Chem.*, 1983, **22**, 2785–2786.
72 S. Yao, Y. Xiong, X. Zhang, M. Schlangen, H. Schwarz, C. Milsmann and M. Driess, *Angew. Chem., Int. Ed.*, 2009, **121**, 4621–4624.
73 M. Di Vaira, M. Peruzzini and P. Stoppioni, *J. Chem. Soc., Chem. Commun.*, 1986, 374–375.
74 E. D. Glendening, C. R. Landis and F. Weinhold, *J. Comput. Chem.*, 2013, **34**, 1429–1437.
75 S. Ye, C.-Y. Geng, S. Shaik and F. Neese, *Phys. Chem. Chem. Phys.*, 2013, **15**, 8017–8030.
76 D. Janardanan, D. Usharani, H. Chen and S. Shaik, *J. Phys. Chem. Lett.*, 2011, **2**, 2610–2617.
77 F. Neese, *Wiley Interdiscip. Rev.: Comput. Mol. Sci.*, 2012, **2**, 73–78.
78 F. Weigend and R. Ahlrichs, *Phys. Chem. Chem. Phys.*, 2005, **7**, 3297–3305.
79 F. Weigend, *J. Comput. Chem.*, 2008, **29**, 167–175.
80 P. Verma, Z. Varga, J. E. Klein, C. J. Cramer, L. Que and D. G. Truhlar, *Phys. Chem. Chem. Phys.*, 2017, **19**, 13049–13069.
81 P. Comba, D. Faltermeier, S. Krieg, B. Martin and G. Rajaraman, *Dalton Trans.*, 2020, **49**, 2888–2894.
82 J. Rezac and P. Hobza, *J. Chem. Theory Comput.*, 2013, **9**, 2151–2155.
83 K. Pierloot, Q. M. Phung and A. Domingo, *J. Chem. Theory Comput.*, 2017, **13**, 537–553.
84 K. Andersson, P. Å. Malmqvist and B. O. Roos, *J. Chem. Phys.*, 1992, **96**, 1218–1226.
85 P. Å. Malmqvist, A. Rendell and B. O. Roos, *J. Phys. Chem.*, 1990, **94**, 5477–5482.
86 C. Angeli, B. Bories, A. Cavallini and R. Cimiraglia, *J. Chem. Phys.*, 2006, **124**, 054108.
87 E. v. Lenthe, E.-J. Baerends and J. G. Snijders, *J. Chem. Phys.*, 1993, **99**, 4597–4610.
88 S. K. Singh, M. Atanasov and F. Neese, *J. Chem. Theory Comput.*, 2018, **14**, 4662–4677.
89 E. A. Pritchina, N. P. Gritsan, O. A. Rakitin and A. V. Zibarev, *Targets Heterocycl. Syst.*, 2019, **23**, 143–154.
90 P. Pollak and F. Weigend, *J. Chem. Theory Comput.*, 2017, **13**, 3696–3705.
91 L. Noodleman, *J. Chem. Phys.*, 1981, **74**, 5737–5743.
92 L. Noodleman and E. R. Davidson, *Chem. Phys.*, 1986, **109**, 131–143.

93 L. Fohlmeister, K. R. Vignesh, F. Winter, B. Moubaraki, G. Rajaraman, R. Pöttgen, K. S. Murray and C. Jones, *Dalton Trans.*, 2015, **44**, 1700–1708.
94 F. Bordwell, J. Cheng, G. Z. Ji, A. Satish and X. Zhang, *J. Am. Chem. Soc.*, 1991, **113**, 9790–9795.
95 A. V. Soudackov and S. Hammes-Schiffer, *J. Phys. Chem. Lett.*, 2014, **5**, 3274–3278.
96 S. Hammes-Schiffer and A. A. Stuchebrukhov, *Chem. Rev.*, 2010, **110**, 6939–6960.
97 A. Sirjoosingh and S. Hammes-Schiffer, *J. Phys. Chem. A*, 2011, **115**, 2367–2377.
98 A. Sirjoosingh and S. Hammes-Schiffer, *J. Chem. Theory Comput.*, 2011, **7**, 2831–2841.
99 S. Hu, S. C. Sharma, A. D. Scouras, A. V. Soudackov, C. A. M. Carr, S. Hammes-Schiffer, T. Alber and J. P. Klinman, *J. Am. Chem. Soc.*, 2014, **136**, 8157–8160.
100 E. Hatcher, A. V. Soudackov and S. Hammes-Schiffer, *J. Am. Chem. Soc.*, 2007, **129**, 187–196.
101 E. Hatcher, A. V. Soudackov and S. Hammes-Schiffer, *J. Am. Chem. Soc.*, 2004, **126**, 5763–5775.
102 R. Send and F. Furche, *J. Chem. Phys.*, 2010, 132.
103 A. Sen, A. Ansari, A. Swain, B. Pandey and G. Rajaraman, *Inorg. Chem.*, 2023, **62**, 14931–14941.
104 M. Ansari, D. Senthilnathan and G. Rajaraman, *Chem. Sci.*, 2020, **11**, 10669.
105 G. Xue, R. De Hont, E. Münck and L. Que Jr, *Nat. Chem.*, 2010, **2**, 400.
106 S. Shaik, H. Chen and D. Janardanan, *Nat. Chem.*, 2011, **3**, 19–27.
107 S. K. Gupta, A. A. Dar, T. Rajeshkumar, S. Kuppuswamy, S. K. Langley, K. S. Murray, G. Rajaraman and R. Murugavel, *Dalton Trans.*, 2015, **44**, 5961–5965.